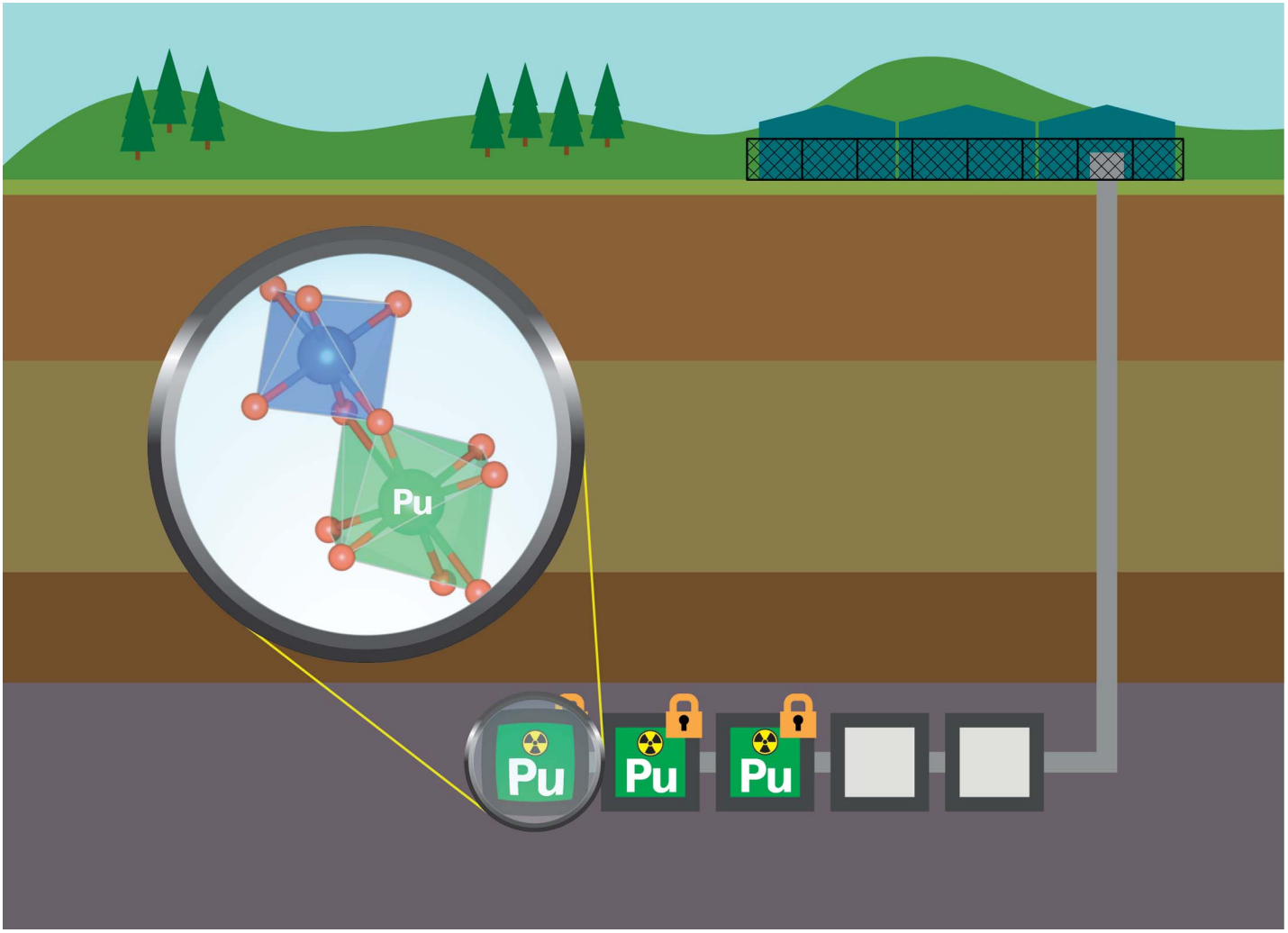

Highlighting research performed by Prof. Sarah Finkeldei, University of California Irvine (USA), formerly Forschungszentrum Juelich, Helmholtz Center, (Germany); Dr Martin Stennett, University of Sheffield, (UK), and Dr Piotr Kowalski and Dr Felix Brandt, Forschungszentrum Juelich, Helmholtz Center, (Germany). We would also like to acknowledge Stephen Birch, at the University of Sheffield, for his assistance with designing the graphic.

Insights into the fabrication and structure of plutonium pyrochlores

This combined experimental and theoretical study demonstrates the capability for pyrochlore structured oxides to accommodate plutonium for safe nuclear waste disposal. Immobilization in a tailored ceramic is considered a promising solution for long-lived radionuclides such as plutonium. This work shows that tetravalent plutonium can be accommodated on the trivalent rare earth site in zirconate pyrochlores such as $Nd_{2-x}Pu_xZr_2O_{7+y}$. The experimental findings, supported by computational studies, indicate that accommodating plutonium causes structural distortions of the cation polyhedra and charge neutrality is maintained by the introduction of oxygen at formerly vacant anion sites.

As featured in:

See S. Finkeldei, M. C. Stennett *et al.*, *J. Mater. Chem. A*, 2020, **8**, 2387.

ROYAL SOCIETY OF CHEMISTRY

rsc.li/materials-a

Registered charity number: 207890

Journal of Materials Chemistry A

PAPER

View Article Online
View Journal | View Issue

Cite this: J. Mater. Chem. A, 2020, 8, 2387

Insights into the fabrication and structure of plutonium pyrochlores†

S. Finkeldei, *[ab] M. C. Stennett, *[c] P. M. Kowalski, [ad] Y. Ji, [ad] E. de Visser-Týnová,[e] N. C. Hyatt, [c] D. Bosbach [a] and F. Brandt [a]

Received 31st May 2019
Accepted 9th August 2019

DOI: 10.1039/c9ta05795a

rsc.li/materials-a

Rare earth zirconates, such as $Nd_2Zr_2O_7$, crystallise with the pyrochlore structure and are a group of materials which have been suggested as potential nuclear waste forms for actinide immobilisation. In this work, a new hydroxide co-precipitation route is presented to investigate the incorporation of Pu into $Nd_2Zr_2O_7$. The plutonium content was varied between 5 and 10 mol% and the structural uptake and Pu oxidation state were probed by X-ray diffraction (XRD), scanning electron microscopy (SEM), and X-ray absorption spectroscopy (XAS). The experimental findings were complemented by DFT *ab initio* calculations. For all the incorporation mechanisms studied PuO_2 was used as the reference reactant state to allow for a direct comparison between the possible Pu uptake scenarios. Analysis of the experimental data suggests that Pu(IV) cations substitute for Nd(III) cations leading to structural distortion of the pyrochlore A-sites. The computed solution energies and bond-distances corroborate the experimental findings and indicate that the excess charge is balanced *via* the introduction of oxygen at formerly vacant sites.

1. Introduction

Due to their unique properties the class of oxides with the pyrochlore crystal structure have been studied for many different applications. These include thermal barrier coatings,[1] solid-oxide fuel cells,[2] and nuclear waste forms for the immobilisation of radionuclides.[3] They are of particular interest for the immobilisation of actinides such as plutonium due to their high chemical flexibility, high tolerance to radiation damage, and high aqueous durability.[4–6] In addition to being a key phase in SYNROC multiphase ceramics,[6] pyrochlores have also been studied as single phase waste forms to immobilise actinide rich waste-streams such as separated plutonium from spent nuclear fuel reprocessing.[7] The pyrochlore crystal structure is a superstructure of the fluorite structure and its general formula can be described as $A_2B_2X_6Y$. Most commonly pyrochlores are of the (3+, 4+) type with rare earth-elements favouring the A-site and 3d, 4d, or 5d transition metals favouring the B-site.[8] (2+, 5+) type pyrochlores can also form but have not been widely studied for application as waste-forms. If the origin of the cubic ($Fd\bar{3}m$) structure is chosen to coincide with the B-site, the A cations occupy the 16d, the B cations the 16c, and the oxygen anions on the X and Y sites the 48f and 8b Wyckoff positions, respectively. In contrast to simple fluorite structured compounds such as ZrO_2, pyrochlores contain combinations of aliovalent cations and the charge compensation required to maintain electrical neutrality occurs *via* the introduction of oxygen vacancies. Pyrochlore structured compounds are missing one eighth of the anions and the resulting oxygen vacancy is localised at the 8a Wyckoff position. The pyrochlore structure can be viewed as being ordered with respect to the fluorite structure. The A-site cations sit in the center of a scalenohedron and are coordinated to six X anions and two Y anions where the cation–anion bond length is slightly shorter. The B-site cations are coordinated solely to six X anions which form a trigonal antiprism around the site. The oxygen deviation parameter x is an indicator of the distortion of the coordination polyhedra surrounding the A and B cations. If x equals 0.375 the A site cations are surrounded by anions arranged as a regular cube and the ideal fluorite structure is observed. For $x = 0.3125$ the B site anion arrangement is regular octahedral which

[a]Forschungszentrum Jülich, Institute of Energy and Climate Research – IEK-6, Nuclear Waste Management and Reactor Safety, 52425 Juelich, Germany. E-mail: sfinkeld@uci.edu

[b]Oak Ridge National Laboratory, Oak Ridge, TN, USA

[c]University of Sheffield, Department of Materials Science and Engineering, S1 3JD, UK. E-mail: m.c.stennett@sheffield.ac.uk

[d]JARA High Performance Computing, Schinkelstrasse 2, 52062 Aachen, Germany

[e]Nuclear Research and Consultancy Group (NRG), Research & Innovation, 1755 LE Petten, The Netherlands

† This manuscript has been authored in part by UT-Battelle, LLC, under contract DE-AC05-00OR22725 with the US Department of Energy (DOE). The US government retains and the publisher, by accepting the article for publication, acknowledges that the US government retains a nonexclusive, paid-up, irrevocable, worldwide license to publish or reproduce the published form of this manuscript, or allow others to do so, for US government purposes. DOE will provide public access to these results of federally sponsored research in accordance with the DOE Public Access Plan (http://energy.gov/downloads/doe-public-access-plan).

corresponds to the ideal pyrochlore crystal structure.[4,9] The pyrochlore structure has been shown to be flexible and will accommodate cations with a variety of ionic radii at the A- and B-sites. Pyrochlores of mixed cationic occupancy can also be formed and these are referred to as non-stoichiometric pyrochlores.[10,11]

Due to the dismantling of nuclear weapon programmes, many countries have large volumes of separated plutonium[12] which may ultimately require immobilisation in a ceramic wasteform. We focus in this study on zirconate pyrochlores because they are known to retain their crystalline structure when subjected to radiation damage; self-irradiation in zirconate pyrochlores leads to the formation of a defective fluorite structure whereas titanate pyrochlore analogues readily amorphise.[13] Moreover, ZrO_2-based pyrochlores show high aqueous durability[14,15] which is another important property for nuclear waste forms. In order to benefit from the inherent advantages of such a crystalline waste form, structural uptake of the radionuclide has to be ensured. Previous studies have probed the uptake of curium at ppm levels on the A site of a zirconate pyrochlore[16] however, to investigate the ability of pyrochlore to serve as potential wasteform for actinides it is important to synthesize materials where the actinide is a major component. Icenhower *et al.* performed dissolution experiments on titanate pyrochlores containing about 12 wt% PuO_2,[5] Nästren *et al.*[17] synthesised $Nd_{1.8}An_{0.2}Zr_2O_7$ (where An = Pu, Am, Np, Th, U) pyrochlores by a liquid infiltration method into porous ceramic beads, and Gregg *et al.*[18] used a modified alkoxide nitrate route to fabricate lanthanum zirconate pyrochlores. To the best of our knowledge, this is the first time a hydroxide co-precipitation route, for the formation of Pu-pyrochlores, has been reported in the literature. A wet-chemical co-precipitation route was adapted with the aim of ensuring homogeneous incorporation of Pu within the pyrochlore crystal structure. Samples doped with 5 and 10 mol% Pu were fabricated and the structural uptake was probed by complimentary experimental techniques (XRD, SEM, and XAS) supported by *ab initio* structural calculations. The data presented here provides new insights into the preferred mechanism of incorporation of Pu within the pyrochlore crystal structure.

Pyrochlore compounds have been extensively investigated by computational methods.[10,19–34] Radiation induced effects such as damage cascade formation,[21–23] amorphization,[30] the energetics of defects formation,[19,24–29,34] and order/disorder transitions[10,20–23,34,35] have been studied, and the results used to support the interpretation of experimental results. Cleave *et al.*[31] and Williford & Weber[32] investigated the incorporation of Pu into a range of rare earth pyrochlore compounds. On the basis of computed solution energies they predicted the incorporation of Pu(III) onto the Nd-site in $Nd_2Zr_2O_7$ as the most energetically preferable mechanism. We have directly tested this prediction in our studies. Recently, Perriot *et al.*[33] have considered the behaviour of Pu(III) and Pu(IV) across pyrochlore-defect fluorite structural interfaces and predicted the preferential segregation of Pu(IV) into the disordered phase. It should be noted that all these studies were performed using a force-field approach with Buckingham-type interaction potentials between atoms. Li *et al.*[34,36] have shown that, although such a force-field based approach often results in reasonable predictions, it can produce defect formation energies that are significantly different from those calculated from *ab initio* methods. Recently, Finkeldei *et al.*[10] have shown that the formation enthalpies and structure of $Nd_xZr_{1-x}O_{2-0.5x}$ pyrochlores can be accurately simulated by density functional theory (DFT)-based *ab initio* methods. Here we use the same approach to support the reported experimental results with the computation of Pu solution energies in $Nd_2Zr_2O_7$ pyrochlore.

2. Experimental section

2.1 Fabrication of plutonium pyrochlore ceramics

The synthesis work described below was carried out in dedicated glovebox lines designed for the handling of alpha-emitting radioisotopes such as plutonium. All samples were prepared by a wet chemical precipitation or co-precipitation approach to obtain highly homogeneous ceramic powders. Aqueous standard solutions of 0.3 mol L^{-1} were prepared from $ZrOCl_2 \cdot 8H_2O$ and $Nd(NO_3)_3 \cdot 6H_2O$ dissolved in de-ionised water. The concentrations of the solutions were checked by inductively coupled plasma optical emission spectrometry (ICP-OES). The precipitation of the hydroxides took place in a glovebox line with an air atmosphere, whereas the thermal treatment was carried out in a furnace in a glovebox line with an argon atmosphere. The Pu precursor used was plutonium nitrate (^{239}Pu) which had been previously characterised by thermal analysis. The weight loss observed occurred in two steps which is in agreement with the reported thermal decomposition of $Pu(NO_3)_4 \cdot xH_2O$ (x = 3, 5) to PuO_2, *via* a plutonylnitrate intermediate.[37,38] The nitrate was found to be X-ray amorphous and on the basis of the former analysis assumed to have a stoichiometry of $Pu(NO_3)_4 \cdot 5H_2O$.[39] Precautions such as acidification of the solutions and direct processing were taken to avoid the formation of a plutonium polymer.

Slight modifications of the Pu-pyrochlore fabrication process led to two different synthesis procedures which are hereafter referred to as synthesis route 1 and synthesis route 2. To obtain highly homogeneous materials, the synthesis of ^{239}Pu-pyrochlore was carried out by a co-precipitation route which was developed by the authors.[40] A stoichiometric $Nd_2Zr_2O_7$ pyrochlore was synthesised at the same time to serve as a reference. To synthesise 4 mmol $Nd_2Zr_2O_7$, 8 mmol of aqueous $Nd(NO_3)_3$ and $ZrOCl_2$ solutions (diluted to a concentration of 0.1 mol L^{-1}) were mixed and transferred (1–3 drops per s) into 100 mL of conc. NH_4OH solution to co-precipitate the hydroxides. The precipitate was separated from the supernatant by centrifuging (4000 rpm, 10 min) and the supernatant was subsequently checked for complete precipitation. Six washing steps were performed on the precipitate, each using 250 mL of deionised water, until the washing water was free of chloride and nitrate. The absence of chlorine and nitrates was confirmed using dipsticks (Macherey-Nagel). The precipitate was transferred into the inert gas glovebox line and dried at 60 °C. After grinding, a calcination step was performed at 600 °C for 2 h with

a heating and cooling rate of 4.8 °C min^{-1}. After a second grinding step two pellets were pressed in a 6 mm die at 707 MPa. The pellets were sintered under reducing atmosphere (Ar-5% H_2) at 1450 °C for 10 h. A heating and cooling rate of 200 °C h^{-1} was used. One of the pellets was subsequently crushed for analysis by XRD.

Synthesis route 1. The appropriate amounts of $Nd(NO_3)_3$ and $ZrOCl_2$ standard solution (Table 1) were mixed and diluted to a concentration of 0.1 mol L^{-1} with deionised water, in a PE bottle ($V = 100$ mL). The desired amount of $Pu(NO_3)_4 \cdot 5H_2O$ was dissolved in 1 mol L^{-1} HNO_3 to yield a 0.1 mol L^{-1} Pu-nitrate solution. First, the Pu-hydroxide was precipitated dropwise in 40 mL liquid ammonia with the help of an Eppendorf pipette. Afterwards, $Nd(OH)_3$ and $Zr(OH)_4$ were co-precipitated by adding the solution *via* a dropping funnel (1 drop per s) to the liquid ammonia which already contained the precipitated Pu-hydroxide. The sample was then washed using the same procedure described above for the $Nd_2Zr_2O_7$ reference material. The calcination and sintering steps were performed under reducing atmosphere (Ar-5% H_2). The pellets were pressed with a 6 mm die at 760 MPa. The sintering parameters are given in Table 2.

Synthesis route 2. In order to further improve the homogeneity of the final product all the metal cations were precipitated simultaneously. The aqueous solutions of $Nd(NO_3)_3$ and $ZrOCl_2$ were acidified to $c(HNO_3) = 1$ mol L^{-1} and mixed prior to the addition of the Pu solution to avoid the formation of a Pu polymer. The desired amount of $Pu(NO_3)_4 \cdot 5H_2O$ (Table 1) was dissolved in nitric acid. At the same time the Pu concentration was reduced to $c(Pu) = 0.01$ mol L^{-1} while the acidity of the nitric acid was kept constant at 1 mol L^{-1}. The light green solution was added slowly to the acidified metal salt solution which was shaken. The mixed metal solution was added into 40 mL concentrated ammonia solution *via* a dropping funnel (1 drop per s). The precipitate was separated using a centrifuge, washed by stirring with deionised water, and dried as described above. Two pellets were pressed, the first was for SEM and XRD characterisation and the second was taken for the XAS measurement. The thermal treatment was carried out according to Table 2.

2.2 Characterisation

The equipment used for the characterisation of the pyrochlores is specified below.

2.2.1 XRD, SEM and EDX. All samples were characterised by XRD using a D2 Phaser (Bruker) diffractometer. The pellets were thoroughly ground prior to measurement. The patterns were recorded from 10–90° 2θ with a step size of 0.01° and an acquisition time of 1 s per step. Subsequent to the XRD analysis the powder from SF-77-P1 was repressed into a pellet and sintered for 5 h at 1450 °C. The resulting $Nd_{1.9}Pu_{0.1}Zr_2O_7$ pellet was investigated by scanning electron microscopy (SEM). The pellet was sputtered with Au–Pd to prevent charging of the specimen during examination. A JEOL 6490 LV operating at a working voltage of 30 kV and a working distance of 10 mm was used to image the pellet microstructure. Elemental analysis was performed by energy dispersive spectroscopy (EDX) with a fixed X-ray acquisition time of 100 seconds.

2.2.2 XAS measurements. XAS data on the $Nd_{2-x}Pu_xZr_2O_7$ samples (where $x = 0.1$ and 0.2) and the plutonium nitrate precursor were carried out at the INE-Beamline of the Angströmquelle Karlsruhe (ANKA).[41] Data for the other Pu reference standards were kindly provided by Vitova *et al.*[42] XANES and EXAFS spectra were recorded at both the Pu L_{III} (18 057 eV) and the Zr K (17 998 eV) edges. The following scanning intervals were used (energy values relative to E_0): −170 eV to −30 eV (step size 5 eV, 2 second integration time), −30 eV to 30 eV (step size 0.5 eV, 2 second integration time), and 30 eV to 12.5k (step size 0.035k, 0.5k integration time). Several scans were taken for each sample and summed to improve the signal-to-noise ratio. Energy calibration of the monochromator was performed by

Table 1 Chemical composition and molar amounts of cations for the samples prepared

Sample	Targeted chemical formula	Synthesis route	*n*(Nd) (mmol)	*n*(Pu) (mmol)	*n*(Zr) (mmol)
SF-70	$Nd_2Zr_2O_7$	1	8	—	8
SF-74-P1	$Nd_{1.8}Pu_{0.2}Zr_2O_7$	1	2.39	0.265	2.65
SF-74-P2	$Nd_{1.8}Pu_{0.2}Zr_2O_7$	1			
SF-77-P1	$Nd_{1.9}Pu_{0.1}Zr_2O_7$	2	1.28	0.0675	1.35
SF-77-P2	$Nd_{1.9}Pu_{0.1}Zr_2O_7$	2			

Table 2 Synthesis conditions for various samples. (h) denotes ramp rate on heating and (c) denotes ramp rate on cooling. * denotes powder repressed into a pellet and sintered again after XRD analysis

Sample	Mass (mg)	Calcination heating rate (°C h^{-1})	Sintering dwell time (h)	Sintering heating rate (°C h^{-1})
SF-74-P1	348.6	200 (h and c)	25	200 (h and c)
SF-74-P2	302.7	200 (h and c)	80	100 (h)/200 (c)
SF-77-P1	80.9	100 (h)/200 (c)	80	100 (h)/200 (c)
			5*	100 (h)/200 (c)
SF-77-P2	179.6	100 (h)/200 (c)	80	100 (h)/200 (c)

collecting spectra from a Zr metal foil; the edge position of the foil (measured at the first inflection in the derivative of the absorption) was aligned to the expected value of 17 998 eV. Due to the overlap of the Pu and Zr absorption edges data was collected in fluorescence mode on sintered pellet samples contained in a double ultra-high-molecular-weight polyethylene (UHMWPE) containment. The INE beamline is a bending magnet beamline which provides an operating X-ray energy range between 2.1 and 25 keV. The optical setup comprises a Ge(422) double crystal monochromator and Rh coated silicon mirrors to focus the beam down to a 500 μm by 500 μm spot. The incident X-ray intensity was measured using a gas filled ionisation chamber and the emitted fluorescence X-ray photons intensity was measured using a 4 element silicon drift detector (Vortex, SII NanoTechnology). For collection of the Zr $K_{\alpha 1}$ fluorescence photons (15 775 eV) the detector was windowed over a range of 15 200–16 300 eV. For collection of the Pu $L_{\alpha 1}$ fluorescent photons (14 288 eV) the detector was windowed over a narrow range between 14 050 and 14 400 eV. The narrow range was required to remove any interference from the Zr K_{α} photons which were contributing a large signal in this energy region due to the high relative concentration of Zr, in relation to Pu, in the samples. No spectra were recorded at a Nd L_{III} edge (7126 eV) due to the high attenuation of low energy X-rays by the sample and the holder.

XAS data on $Nd_2Zr_2O_7$ and the Zr reference standards were collected at the Zr K edge on beamline X23A2 of the now decommissioned National Synchrotron Light Source (NSLS) at the Brookhaven National Laboratory (BNL). The following scanning intervals were used (energy values relative to E_0); −200 eV to −20 eV (step size 1 eV, 1 second integration time), −20 eV to 30 eV (step size 0.3 eV, 1 second integration time), and 30 eV to 15k (step size 0.05k, 0.5k integration time). Energy calibration of the monochromator was performed by collecting spectra from a Zr metal foil; the edge position of the foil (measured at the first inflection in the derivative of the absorption) was aligned to the expected value of 17 998 eV. Data were acquired in transmission mode using finely ground powder specimens dispersed in polyethylene glycol (PEG) to give a thickness of one absorption length. X23A2 consisted of an unfocused bending magnet beamline (4.9 to 32 keV) with an optics setup incorporating a Si(311) monochromator with a fixed exit Golovchenko–Cowan design, and a single bounce flat Rh-coated harmonic rejection mirror. Slits were employed to reduce the beam size to 7 mm in the vertical and 0.5 mm in the horizontal. The incident and transmitted X-ray intensities were measured using gas filled ionisation chambers.

All raw data was processed using the Athena software and EXAFS analysis was performed using FEFF6 and the Artemis program.[43] The Zr k-edge data was corrected for self-absorption using the Troger algorithm.[44] The Pu L_{III} edge data was not corrected as self-absorption is not a concern when working in the dilute limit.[45]

2.2.3 Bond-valence-sum calculations. The bond valence concept provides validation of a crystal structure model by comparison of the formal oxidation state (V_i) with the bond valence sum. According to Brown–Altermatt[46] the bond valence sum is given by:

$$V_i = \sum_j \exp\left(\frac{r_0 - r_{ij}}{B}\right) \quad (1)$$

where r_{ij} and r_0 are the observed and tabulated bond lengths, between the atoms i and j and B is an empirical constant (usually 0.37 for oxides). Reference bond lengths were taken from Zachariasen.[47]

2.3 Molecular simulation

The atomistic modelling studies of Pu incorporation into the $Nd_2Zr_2O_7$ pyrochlore structure were performed using the density functional theory (DFT)-based Quantum-ESPRESSO simulation package.[48] In order to make reliable predictions of the energetics of Pu incorporation the PBE exchange–correlation functional was applied.[49] This methodology has previously been successfully employed in studies of actinide containing systems[50,51] and $Nd_xZr_{1-x}O_{2-0.5x}$ pyrochlores-type compounds, including $Nd_2Zr_2O_7$.[10,34] As in these previous studies, the PBEsol functional[52] was used to obtain better geometries of selected atomic configurations. The core electrons of the constituent atoms were modelled with ultrasoft pseudopotentials[53] and the $6s^2$ $6p^6$ $6d^2$ $7s^2$ electrons (plus 5f electrons in DFT + U calculations) of the Pu atoms were computed explicitly. Based on previous experience in computing f elements-bearing systems, 50 Ryd was selected as the plane-wave energy cut-off.[51] Pu has strongly correlated 5f electrons therefore the correlation effects were computed using the DFT + U approach as a correction to the regular DFT calculations. This approach has previously been successfully applied to simulate $Nd_xZr_{1-x}O_{2-0.5x}$ pyrochlore-type systems[10] however, because the computed correlation effects for Nd atoms in $Nd_2Zr_2O_7$ are negligibly small,[10] the focus in this study was on the correlation effects associated with the Pu atoms only. The Hubbard U parameter values for Pu(III) and Pu(IV) applied in this study were 2.0 eV and 2.7 eV, respectively. These representative values were taken from Beridze *et al.*[51] and were derived from a series of Pu-bearing compounds using the linear response method.[54]

Following our methodology from previous studies,[10,34,36] the $Nd_2Zr_2O_7$ pyrochlore structure was represented by an 88 atoms cubic supercell and calculations were performed on the 2 × 2 × 2 Methfessel–Paxton k-point grids.[55] The solution energies of the Pu atoms was computed assuming the following reactions:

Incorporation of Pu(III) on the Nd (A) site:

$$PuO_2 + A_A^{\times} \rightarrow Pu_A^{\times} + 1/2A_2O_3 + 1/4O_2 \quad (2)$$

Incorporation of Pu(III) on the Zr (B) site:

$$2PuO_2 + 2B_B^{\times} + O_O^{\times} \rightarrow 2Pu_B' + V_O'' + 2BO_2 + \frac{1}{2}O_2 \quad (3)$$

Incorporation of Pu(IV) on the Zr (B) site:

$$PuO_2 + B_B^{\times} \rightarrow Pu_B^{\times} + BO_2 \quad (4)$$

Incorporation of two Pu(IV) on the Nd (A) site with subsequent introduction of an oxygen atom on an oxygen vacancy site:

$$2PuO_2 + 2A_A^{\times} \rightarrow 2Pu_A^{\bullet} + O_v'' + A_2O_3 \quad (5)$$

Incorporation of three Pu(IV) on the Nd (A) site with subsequent introduction of one Nd vacancy:

$$3PuO_2 + 4A_A^{\times} \rightarrow 3Pu_A^{\bullet} + V_A''' + 2A_2O_3 \quad (6)$$

Incorporation of Pu(III) on the Nd (A) or Zr (B) site *via* the reduction of Pu(IV):

$$PuO_2 + A_A^{\times} + 1/2H_2 \rightarrow Pu_A^{\times} + 1/2A_2O_3 + 1/2H_2O \quad (7)$$

$$2PuO_2 + 2B_B^{\times} + O_O^{\times} + H_2 \rightarrow 2Pu_B' + V_O^{\bullet\bullet} + 2BO_2 + H_2O \quad (8)$$

In all the above reactions the reference reactant state chosen for Pu was PuO_2. Reactions (2), (3), (7) and (8) would only be relevant under reducing synthesis conditions such as those used during this study. The rationale behind using the same Pu reference state for all reactions was to allow direct comparison of the resulting reaction enthalpies. This approach differs from previous reported modelling studies,[31–33] in which Pu_2O_3 has been used as the reference for reactions involving incorporation of Pu(III). Because different pseudopotentials were applied for Pu(III) and Pu(IV) when performing DFT calculations with 5f electrons included in the pseudopotential core, we used Pu_2O_3 as the reference for reactions leading to the formation of Pu(III). However, because PuO_2 was used as the reference reactant in all of the above mentioned reactions, the standard enthalpy difference between Pu_2O_3 and PuO_2 of 232 kJ mol^{-1} (ref. 56) was added to the relevant reaction enthalpies computed with Pu_2O_3. To obtain solution energies for reaction (7) and (8) the standard formation enthalpy of water gas (−241.8 kJ mol^{-1} = −1.25 eV) was added to the solution energies of reactions (2) and (3), respectively. In order to find the most energetically favourable Pu incorporation mechanism, allowed by the 88 atoms supercell, Pu incorporation configurations were calculated.

The presence of a Pu(IV) species was reported by Toth *et al.*[57] for 0.05 mol L^{-1} $Pu(NO_3)_4$ in 0.11 M HNO_3. Disproportionation reactions led to the presence of additional Pu species so the $Pu(NO_3)_4$ was always freshly dissolved in 1 M HNO_3 prior to being used. Calculations of the thermodynamic equilibrium Pu species were carried out with GEMS using the NAGRA-PSI database,[58] according to the experimental conditions of synthesis route 1 in the presence of 1 kg water. The calculations indicated aqueous plutonyl PuO_2^{2+} to be the predominant species. It should be noted however, that the GEMS calculations can only predict the thermodynamic equilibrium and no kinetic effects of the reaction are taken into account. Clark *et al.*[59] reported Pu(IV) to be unstable if it comes into contact with oxygen but the rate for this reaction was found to be negligible. The presence of Pu(VI) has also been described by Glazyrin *et al.*[60] in 1–5 M HNO_3 at 90 °C. In the present study the presence of Pu(VI) was not expected as the solutions were always freshly prepared prior to each synthesis and directly consumed. The disproportionation reaction of Pu(IV) in acidic solutions is given below:

$$3Pu^{4+} + 2H_2O \leftrightarrow 2Pu^{3+} + PuO_2^{2+} + 4H^+ \quad (9)$$

The fourth order dependence of the disproportionation on $[H^+]$ makes this reaction highly unlikely to occur. Under strongly acidic conditions[59] there was no experimental observation for the disproportionation reaction having taken place. Therefore, the dissolution of $Pu(NO_3)_4$ in 1 M HNO_3 at room temperature is assumed to result in a Pu(IV) solution. In addition, sintering of the resulting powders takes place under reducing conditions which makes the oxidation state in the solution less critical for the final product.

For both synthesis routes all thermal treatments were carried out under reducing atmosphere to promote the reduction of Pu(IV) to Pu(III) and inhibit the formation of PuO_2 as a discrete phase. For synthesis route 2 the sintering duration was extended to 80 h, because the kinetics of the reduction of Pu(IV) to Pu(III) and the incorporation mechanism of Pu into the pyrochlore structure are not well understood. Two $Nd_2(Zr_{1.9}Pu_{0.1})O_7$ pellets were pressed and sintered for 80 h to reduce the plutonium to Pu(III). One of the pellets was ground and the

3. Results and discussion

3.1 Synthesis routes and X-ray diffraction (XRD)

Synthesis route 1 involved precipitation of the plutonium hydroxide prior to Nd- and Zr-hydroxide formation; this allows the two steps to be studied separately. However, to allow for a co-precipitation of all three hydroxides and the formation of a homogeneous precursor at the molecular level, the metal salt solutions of plutonium, neodymium and zirconium were mixed prior to precipitation, in synthesis route 2. The Nd- and Zr-metal salt solution was acidified and the concentration of the Pu-solution was reduced to c(Pu) = 0.01 mol L^{-1}. All thermal treatments were carried out under reducing conditions with the intention to reduce Pu(IV) to Pu(III), which should occupy the A-site in pyrochlore.

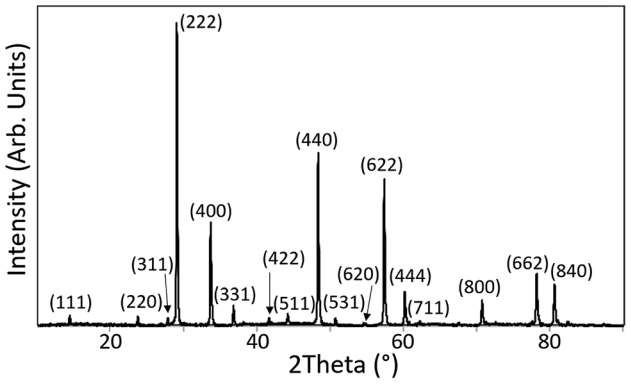

Fig. 1 XRD pattern of $Nd_{1.9}Pu_{0.1}Zr_2O_7$ which was synthesised according to synthesis route 2.

powder characterised by XRD. The XRD patterns obtained for the pure $Nd_2Zr_2O_7$ compound and 5 and 10 mol% Pu doped compounds contained reflections which could all be attributed to a pyrochlore structured phase. Fig. 1 shows the pattern acquired from $Nd_{1.9}Pu_{0.1}Zr_2O_7$ which is representative of all the samples. The powder was subsequently pressed and re-sintering to be used for SEM characterisation.

Previous studies in the literature concerning the fabrication of plutonium pyrochlores lack a thorough analysis of both the structural incorporation and the oxidation state of Pu. Kulkarni *et al.*[61] prepared a $Pu_2Zr_2O_7$ pyrochlore *via* a solid state route under helium atmosphere. They ascribed an observed weight loss between 1000–1400 °C to the reduction of Pu(IV) to Pu(III) driven by oxidation of graphite present in the system. They observed a linear decrease of the lattice parameter in the series $(Pu_xLa_{1-x})_2Zr_2O_7$ (where $x = 0.0$–1.0) with an increase in Pu content. This is consistent with a reduction in the average size of the A-site cation, because both Pu(IV) and Pu(III) have a smaller ionic radius in eightfold coordination than La(III). Although the authors stated that a weight gain could be observed when the samples were re-oxidised no direct measurement of the Pu oxidation state was provided. Burakov *et al.*[7] reported the fabrication of Pu-238 doped titanate pyrochlores *via* a modified solid state route. A plutonium nitrate solution was added to a mixture of inactive oxide precursors and subsequently calcined and sintered in air. No specific details were provided in the publication but it is assumed that denitration of the plutonium nitrate occurred yielding PuO_2, prior to a further solid state reaction resulting in the formation of the target phase. There was no characterisation of the plutonium oxidation state or structural environment and based on the analysis provided it is unclear as to whether the samples were homogenous.

3.2 Scanning electron microscopy (SEM) and energy dispersive X-ray spectroscopy (EDX)

The $Nd_{1.9}Pu_{0.1}Zr_2O_7$ pellet prepared *via* synthesis route 2, was further characterised by SEM and EDX. Fig. 2(a) shows a secondary electron (SE) image of the pellet surface; the areas where EDX spot measurements were made are marked. The elemental distribution was probed by mapping the surface of the pellet. The maps are shown in Fig. 2(c–e) and they indicate a homogeneous distribution of Pu, Zr, and Nd. The surface imperfection, visible on the right side of the pellet in Fig. 2(a), is either an artefact of the sintering process or material deposited during the surface coating process. It was not possible to prepare the surface of the sample using metallographic techniques prior to the analysis but there was no indication that this region was chemically dissimilar to the rest of the pellet.

EDX measurements of the composition, at the four spots of interest in Fig. 2(a) indicated a mean Pu content of 5.4 at%, and that the Pu was distributed homogeneously at locations 1, 2 and 3 within the limit of sensitivity for the technique. The measurement at location 4 was taken from an agglomeration of ceramic grains, with a diameter of about 40 μm, located in the cavity shown Fig. 3(d). The plutonium content at this location was 7.8 at% which is approximately one and a half times higher than the value measured at locations 1, 2, and 3. The microstructure of the four locations were subsequently characterised in more detail. Fig. 3(a–c) show location 1 at three different magnifications. The microstructure is composed of primary grains between 1–5 μm in diameter as seen in Fig. 3(c). The pellet surface appears porous and is covered with small grains. This may be caused by the grinding of the pellet and the relatively short sintering time of 5 h after the repressing step. The difference in the brightness of the smaller grains, with respect to the larger ones, is related to non-uniformities in the conductive surface coating.

There is no indication of any gross differences in chemical composition, or the presence of any secondary phases in the sample, which is consistent with the XRD analysis and confirms that a single phase Pu-pyrochlore has been formed.

The wet-chemical synthesis routes, used in this work, could plausibly result in three possible scenarios for the charge and position of plutonium within the pyrochlore crystal lattice:

(1) The synthesis conditions will promote reduction of Pu(IV) in the starting precursor and formation of a pyrochlore with Pu(III) on the A-site. Nästren *et al.*[17] reported the formation of a single phase Pu-doped neodymium pyrochlore, containing Pu(III), under reduction conditions (Ar/H_2). It was not indicated whether the Pu was added in the tri- or tetra-valent state so it is unclear as to whether the processing environment had driven the reduction from Pu(IV) to Pu(III) or simply stabilised the Pu(III) already present. This processing route led to Pu(III) being accommodated in eightfold coordination at the A-site in the pyrochlore structure with no charge compensation required. Gregg *et al.* reported the synthesis of $La_{1.9}Pu_{0.1}Zr_2O_7$ *via* a modified alkoxide route using PuO_2 dissolved in nitric acid and observed the formation of a near single phase pyrochlore with Pu(III) present at the A-site.[18]

(2) The kinetics of the pyrochlore crystallisation process may be faster than the reduction of the Pu in the precursor from Pu(IV) to Pu(III). This could lead to the formation of the pyrochlore with Pu(IV) occupying the A-site. It is also plausible that Pu(IV) could be incorporated onto the B-site however this would require substitution of Zr onto the A-site which seems unlikely based on the relative ionic size difference between Nd(III) and Zr(IV) in eightfold coordination.

(3) The synthesis conditions are inadequate to reduce Pu(IV) to Pu(III) during the thermal treatment. In this case Pu(IV) could occupy either the A-site or the B-site. Mixed occupancy of both sites is also possible.

To resolve these questions EXAFS and XANES measurements were carried out at the ANKA-INE beamline. Complimentary atomistic simulation studies were also performed.

3.3 XAS

Plutonium L-edge XANES. Normalised L_{III}-edge absorption spectra for the $Nd_{1.9}Pu_{0.1}Zr_2O_7$ (SF-77) and $Nd_{1.8}Pu_{0.2}Zr_2O_7$ (SF-74) plutonium doped samples are shown in Fig. 4. Overlaid with the sample data are standard data from two solutions (1 M $HClO_4$) containing Pu(III) and Pu(IV)[42] and the original $Pu(NO_3)_4$

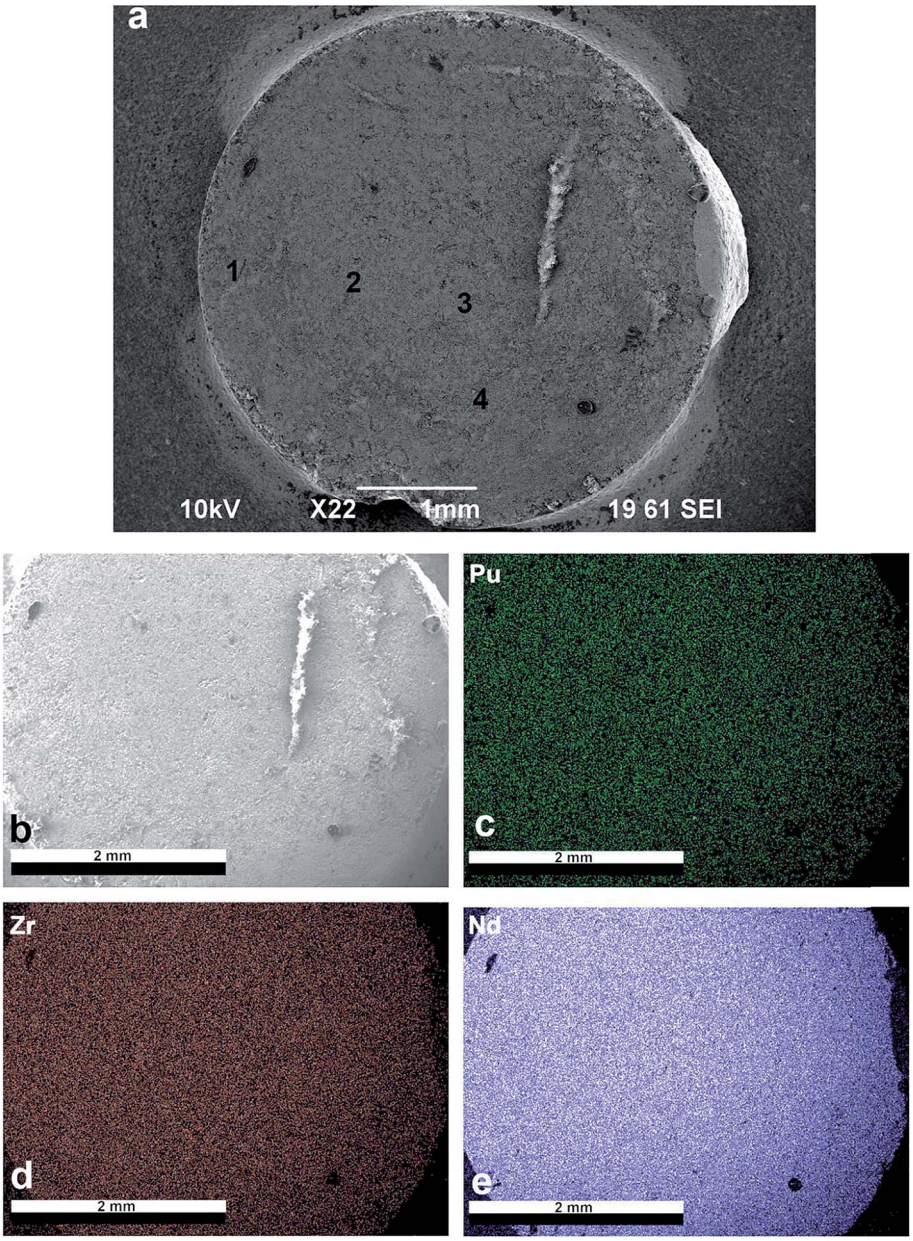

Fig. 2 (a) SE image of the coated pellet (synthesis route 2) where the numbers indicate the regions where EDX measurements were made; (b) overview of the pellet for elemental EDX mapping; (c) Pu distribution; (d) Zr distribution; (e) Nd distribution. In total 20 frames were collected for the EDX mappings. Adapted from ref. 40.

starting material. In contrast to first row transition metals the XANES region of actinide L-edge spectra do not contain many features making them relatively easy to interpret. The spectra for tri- and tetra-valent compounds tend to be similar in appearance and consist of a single broad absorption peak with smooth rising and falling edges, and a second broad feature at approx. 45 eV above the white line. Because of the lack of features the principle characteristics typically reported are the energy of the peak on the white line and the absorption edge energy (determined from the inflection point on the edge).[62] For all data a pre-edge background subtraction was performed and the edges were normalised allowing the edge and peak positions to be measured.[45] As shown in Fig. 4(a) there is a shift in the energy position of the maximum on the white line with a reduction in the Pu oxidation state. Fig. 4(b) shows the first derivative of the normalised absorption where the inflection point (edge position) on the rising edge of the white line is given by the first maximum. A clear shift in the position of the maximum in the first derivative can be seen between the two standard solutions. Values for the peak energy and the absorption edge energy for the samples and standards are given in Table 3.

The absorption edge energy is primarily determined by the charge of the central Pu atom although the exact position, and

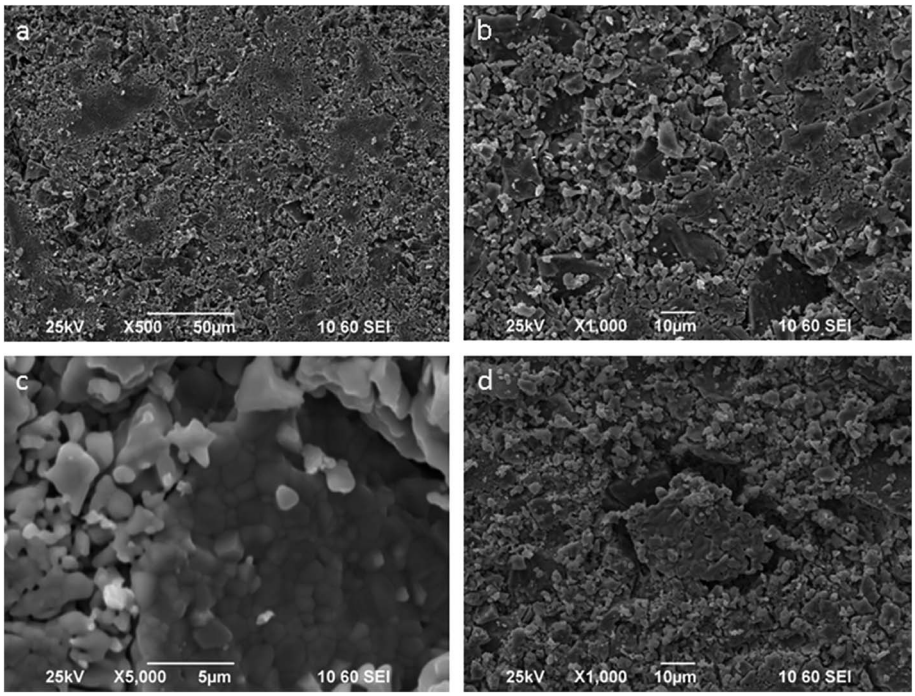

Fig. 3 (a–c) SE images of location 1 taken at different magnifications; (d) magnification of location 4. Taken from ref. 40.

shape, will be modified by the degree of electron transfer to the surrounding ligands. In the case of the lower valence actinides (Act) there is a monotonic increase in the energy of the absorption edge with valence however a discontinuity arises between Act(IV) and Act(V) which is related to the formation of *trans*-dioxo species.[63,64] For the case of Pu aquo-complexes (prepared in 1 M $HClO_4$) clear differences in the shape of the near-edge spectra for the dioxo-containing species were reported.[65] Multiple scattering (MS) events along the dioxo-species give rise to a feature at approximately 15 eV above the white line which has also been well documented in U and Np compounds.[66,67] The absence of this feature in our data indicates that no short Pu–O bonds are being formed and excludes the presence of dioxo-species in these samples. The shape of the

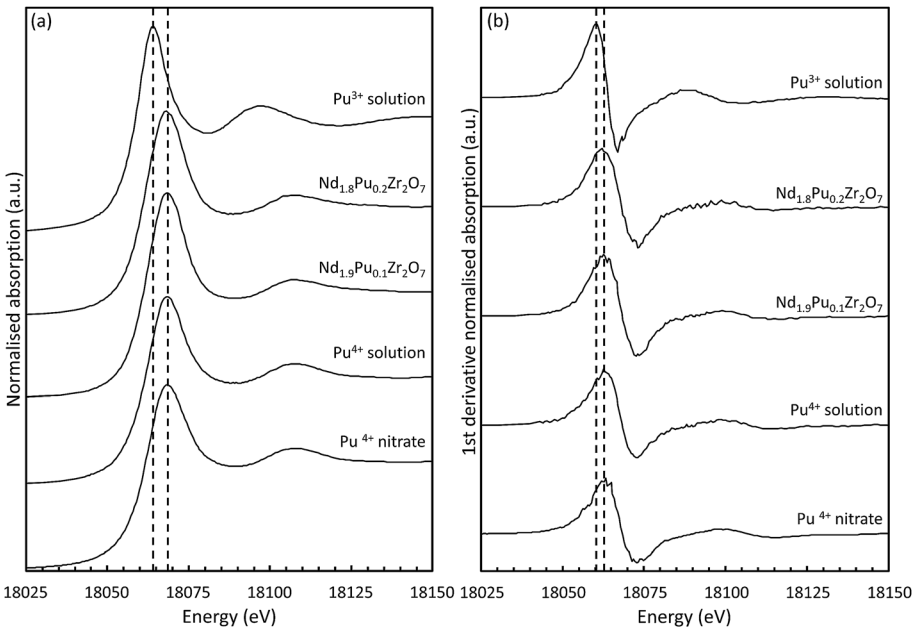

Fig. 4 (a) Normalised absorption spectra of the pyrochlore samples compared to the two liquid plutonium standards and the original $Pu(NO_3)_4$ starting material;[42] (b) first derivative of the Pu L_{III} absorption edge for the samples and standards.

Table 3 Measured peak and edge energies for standard solutions and the pyrochlore samples. Values for Pu solutions were provided by T. Vitova[42]

Compound	Edge energy (eV)	Peak energy (eV)	Valence state
Pu(III) 1 M $HClO_4$; [Pu] 30 mM	18 060.2	18 064.1	3
$Pu(NO_3)_4$ precursor	18 063.4	18 068.6	4
Pu(IV) 1 M $HClO_4$; [Pu] 30 mM	18 065.1	18 068.9	4
Pu(IV) 1 M $HClO_4$; [Pu] 4 mM	18 063.9	18 068.9	4
$Nd_{1.9}Pu_{0.1}Zr_2O_7$	18 063.4	18 068.7	3.98
$Nd_{1.8}Pu_{0.2}Zr_2O_7$	18 062.8	18 068.4	3.92

edge is sensitive to both the local coordination environment and the electronegativity of the connecting ligands. The features in the Act L_3 XANES are therefore determined, to some extent, by the photoelectron scattering paths and not simply by the occupancy of the 6d electronic orbitals.[62] It is therefore necessary to select appropriate standards and the correct methodology for assigning valence; comparison of data from a range of aquo-, aquochloro-, aquonitrato-, and carbonato-complexes indicated that the shift in the inflection point on the absorption edge is far more sensitive to changes to the extended chemical environment than the valence of the central Pu cation.[62] These changes can influence the interpretation of unknown compounds; asymmetry in the white line will influence the determination of the edge energy, from the first inflection point on the absorption edge, and care should be exercised to allow unambiguous assignment of the valence state. Soldatov *et al.* demonstrated this effect in tertiary U oxides.[68] As can be seen in Table 3 there is a wide spread in the edge energy position for the Pu(IV) standards but the peak energies are more tightly clustered. It was therefore decided to determine the oxidation state of the samples from the peak energy. An average peak energy was calculated for the Pu(IV) standards and a linear change in peak position with oxidation state was assumed. The results presented here for the standards are in good agreement with those published previously.[18,65] The tabulated values for the sample oxidation states were then determined by interpolation; the results indicate that for both pyrochlore samples the majority of the Pu is the tetravalent oxidation state, which is unexpected given that the samples were fired under reducing conditions. The isostructural $Pu_2Zr_2O_7$ and $Am_2Zr_2O_7$ compounds are known to form when heated under a hydrogen (4% in Ar) atmosphere at 1500 °C (10–20 hours dwell time).[69] Shoup *et al.*[70] described the synthesis of monoclinic $Pu_2Ti_2O_7$ by solid state reaction under the same atmosphere. PuO_2 was used as a starting material and TiN was used as a titanium source. The combination of the reducing agent (TiN), a reducing atmosphere, and long heating times resulted in the Pu being stabilised in the Pu(III) oxidation state. Gregg *et al.* reported an almost complete reduction of the plutonium in $(La_{1.9}Pu_{0.1})Zr_2O_7$ when synthesised under hydrogen (N_2–3.5% H_2) at 1450 °C (24 hours dwell time).[18] Similar results were also reported by Naestren at low dopant concentration although they used a significantly higher sintering temperature (1650 °C) and a metal furnace.[17] Although our findings differ from previously published results it is worth considering the fact that differences in Pu content, processing conditions, and heat treatment parameters will have an effect on the final Pu oxidation state. It should also be noted that the experimental results are consistent with the results of the molecular modelling (Section 3.4). These suggest that the most energetically favourable mechanism is for the Pu to be incorporated as Pu(IV) on the Nd(III) site with the introduction of oxygen atoms into oxygen vacancy sites.

Zirconium k-edge XANES. Spectra from a group of Zr containing crystalline standards are shown in Fig. 5(a). For all data a pre-edge background subtraction was performed and the edges were normalised allowing a value for the edge position to be measured; the edge position is herein defined as the energy half way up the absorption edge (*i.e.* at a normalised absorption value of 0.5). These compounds were chosen to represent the variety of different characteristic first shell environments that can be found around Zr in mineral systems. It should be noted that the spectra presented here are consistent with those already published previously.[71–74] Synthetic zircon, $ZrSiO_4$ (Acros Organics 99%), is a model for Zr in eight-fold coordination.[75] Zr occurs in a disordered seven-fold coordinated site in baddeleyite (ZrO_2)[76] where all seven Zr–O bonds are of different length. The baddeleyite used in this study was synthetic reagent grade monoclinic zirconia (Sigma-Aldrich 99%). Zirconia undergoes high temperature phase transitions to tetragonal and cubic structures which can be stabilised at room temperature using oversized dopants such as Y or Ca. In this study synthetic yttria-stabilised zirconia (Tosoh Corporation 99%) and calcium-stabilised zirconia (synthesised in house from ZrO_2 and $CaCO_3$; both Sigma-Aldrich 99%) were measured. The transformation process involves the distortion of the Zr–O nearest neighbour shell and fully stabilised cubic zirconia solid solutions contain seven-fold coordinated Zr.[77] Zr in six-fold coordination is common in Zr-bearing alkali silicate minerals such as zektzerite ($LiNaZrSi_6O_{15}$)[78] and catapleiite ($Na_2ZrSi_3O_9 \cdot 2H_2O$);[79] the coordination polyhedral in these samples is a nearly regular octahedron. The final standard measured was synthetic $BaZrO_3$ (synthesised in house from ZrO_2 and $BaCO_3$; both Sigma-Aldrich 99%) which has the ideal cubic perovskite structure where the Zr atoms are situated in regular octahedra.

Inspection of the K-edge XANES region of the spectra from these materials shows marked differences in the shape and relative intensity of the individual components of the doublet (indicated by a and b in Fig. 5(a)) on the absorption edge.[72] The octahedrally coordinated Zr standard ($ZrSiO_4$) is characterised

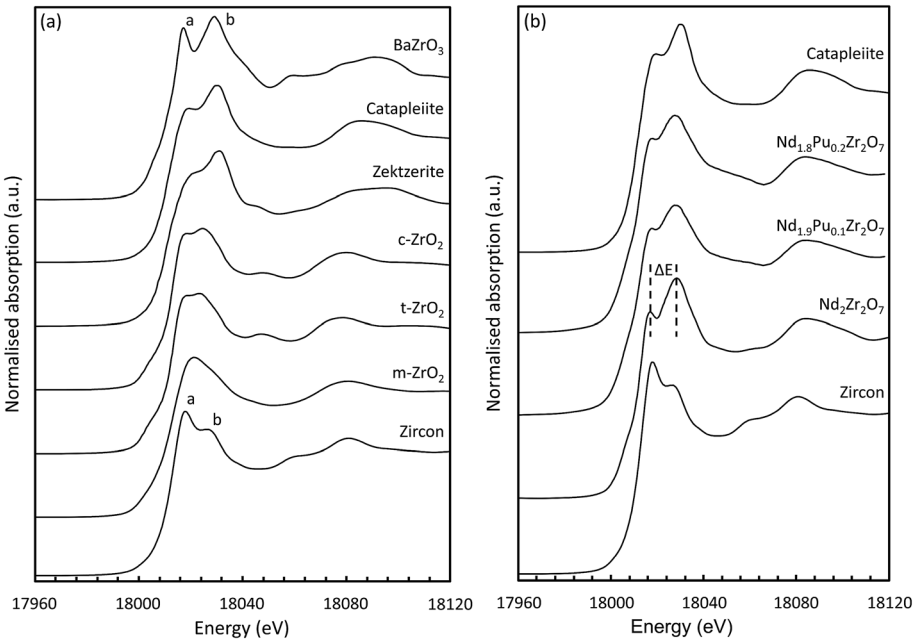

Fig. 5 (a) Zirconium k-edge XANES spectra for standard compounds; (b) selected standards overlaid with the data from the pyrochlore samples.

by a larger intensity component on the low energy side of the doublet whilst for the six-fold coordinated standard ($BaZrO_3$) the component on the high energy side is more intense. These two features appear at approx. 6 and 15 eV above the position of the edge (E_0) and can be used as a qualitative diagnostic for the average coordination environment of the Zr. When Zr is situated in a highly centro-symmetric environment then the splitting between the two features is far more pronounced; this can be seen clearly in the data obtained from the $BaZrO_3$ sample. Lee *et al.* observed that the splitting (ΔE) increased with increasing crystal symmetry in $Gd_2Zr_2O_7$ samples prepared by the Pechini method and processed at different temperatures.[80] Samples processed at lower temperatures adopted a more disordered structure and had a smaller ΔE. Similar trends were shown by Li *et al.*[77] in their study on different zirconia polytypes, indicating that the k-edge absorption spectra provide a useful tool for studying order/disorder. Changes in the relative intensity of the two features also indicate a change in the local Zr structural environment. In the yttria doped zirconia system a slight increase in the relative intensity of a in conjunction with a small shift in b to lower energy was characteristic of an increase in the average Zr–O coordination number.[81]

Data acquired at the Zr k-edge for the pyrochlore samples ($Nd_{2-x}Pu_xZr_2O_7$; where x = 0.0, 0.1, and 0.2) are shown in Fig. 5(b) together with the reference spectra from catapleiite and zircon. All three spectra show a marked similarity to catapleiite indicating that the Zr is six-fold coordinated. This result is consistent with the expected crystal structure for $Nd_2Zr_2O_7$,[82] and the X-ray diffraction results presented in Section 3.1. Semi-quantitative inspection of the spectra shows that the splitting between the two features is reduced for the Pu doped samples suggesting that the local Zr environment is being distorted by the introduction of Pu cations on the A-site in the pyrochlore structure. This is not unexpected given the 13.3% difference in ionic radii, between eight-fold coordinated Nd(III) (I_R = 1.109 Å) and Pu(IV) (I_R = 0.962 Å).[83] A small contraction in the average size of the A-site alongside an increase in the local structural distortion would be anticipated when Nd is replaced with smaller Pu cations. Changes in the relative intensity of the a and b features are also observed with increasing Pu content consistent with the introduction of Pu(IV) on the Nd(III) site and subsequent charge balance by the filling of oxygen vacancies associated with the Zr.

Plutonium L_{III}-edge EXAFS. Analysis of the extended X-ray absorption fine structure (EXAFS) can reveal information about the local structural environment surrounding different atoms within crystalline and amorphous materials. Confirmation of both the number of next nearest neighbours (coordination number) and also the scattering path length (approximately equal to twice the bond distance) between an atom and those neighbours can be obtained. In well-ordered systems information can also be obtained about more distant coordination shells allowing a more detailed description of the local structure around a particular set of atoms.

The local structural environment around the Pu atoms was investigated by quantitative analysis of the EXAFS region of the Pu L_{III}-edge data. In order to refine the contact distances, between the central absorbing Pu atoms and the nearest neighbour coordination shells, a structural model was required. The structure of rare earth zirconate pyrochlores are well reported in the literature; in this study the structure of $Nd_2Zr_2O_7$ refined by Harvey *et al.*[82] was used as the starting model. The Pu was targeted for incorporation on the A-site of the pyrochlore structure which is characterised as having eight nearest neighbours; six longer A–O_{48f} bonds and two shorter A–O_{8b} bonds. As a first approximation, a structural model containing

two scattering paths was used to represent the two different A–O bond lengths. The degeneracies of the paths were weighted accordingly and a mean square displacement parameter σ^2(O1) was used to model the thermal vibrations of the nearest neighbour oxygens. The amplitude reduction factor ($S_0{}^2$) and the shift in the edge energy (ΔE_0) were also allowed to vary. It should be noted at this stage the fitted k and R ranges were restrained to only model the signal in the FT $k^3\chi(k)$ at approx. 1.8 Å (uncorrected for phase shift). This model gave a fit to the data which was deemed unacceptable due to the large refined value of ΔE_0 and negative mean square displacement parameters. This result suggests that the Pu first shell environment is significantly distorted from that of the classic pyrochlore A-site structural motif. The degeneracies of the two Pu–O1 paths were then inverted to give six short Pu–$O1_s$ paths and two longer Pu–$O1_l$ paths. This approach yielded a reasonable fit with sensible values for the $S_0{}^2$, ΔE_0, and the mean square displacement parameters. In order to confirm the robustness of the model the electron reduction factor $S_0{}^2$ was fixed at the value refined previously, and the degeneracy of the two Pu–O1 paths were allowed to vary. This method returned a fit where the degeneracies converging towards six for the short Pu–$O1_s$ path and two for the longer Pu–$O1_l$ path. For completeness, an attempt to fit a single oxygen shell around the Pu was made. Fitting a structural environment like Zr in $Nd_2Zr_2O_7$ failed returning an unacceptably large $S_0{}^2$ and a negative mean square displacement parameter. Efforts to fit a single environment with eight nearest neighbour oxygen atoms were also unsuccessful, indicating that the environment around the Pu atoms is significantly distorted.

In order to satisfactorily fit the spectral features at higher radial distance, additional scattering paths were added to the model. This took into account the Pu–Nd, Pu–Zr1, Pu–O2, Pu–O3, Pu–Zr2, and Pu–O4 scattering paths; where applicable an appropriately weighted scattering path was chosen to model all like atom pairs at similar distances. Fractional occupancy of plutonium was incorporated by inclusion of a Pu–Pu scattering path. The available scattering paths are generated by the FEFF algorithm which uses *ab initio* theory to calculate multiple scattering paths based on a given structural model.[84] The structural model used is taken from a crystallographic input file often referred to as a CIF.[85] In order to allow FEFF to generate the additional Pu–Pu scattering path the CIF was modified by changing one of the six second shell neighbours from a Nd atom to a Pu atom. This change alone would result in a fractional occupancy of 0.167 formula units Pu on the A-site. In order to correctly model the fractional occupancy, the contribution (amplitude) of the resulting Pu–Pu scattering path was multiplied by a factor of $x/(1/6)$ and the Pu–Nd scattering paths were multiplied by a factor of $(1-x)/(5/6)$, where x is the fraction of Pu atoms on the A-site.

This produced a model which afforded a good fit (R-factor = 2%) to the main features in both the $k^3\chi(k)$ waveform and the FT $k^3\chi(k)$ spectral envelope out to a k of 11 $Å^{-1}$ and an R of 5.5 Å, respectively. The fits to both data sets are shown in Fig. 6 and the refined model parameters are shown in Table 4. The data were modelled with thirteen independent variables: two variables related to the overall EXAFS scattering process ($S_0{}^2$ and E_0) and eleven variables related to nine independent single scattering path lengths and associated mean squared displacement parameters. The average nearest neighbour Pu–O bond lengths were determined to be 2.35 Å ± 0.03 for $Nd_{1.9}Pu_{0.1}Zr_2O_7$, and 2.33 Å ± 0.03 for $Nd_{1.8}Pu_{0.2}Zr_2O_7$. These values are smaller than the weighted mean Nd–O bond length (2.52 Å) from the crystal structure published by Harvey *et al.*[82] although this is sensible given that the ionic radius of Pu(IV) in eight-fold coordination (0.962 Å) is smaller than that of Nd(III) (1.109 Å).[83] Independent validation of the refined path lengths can be performed using

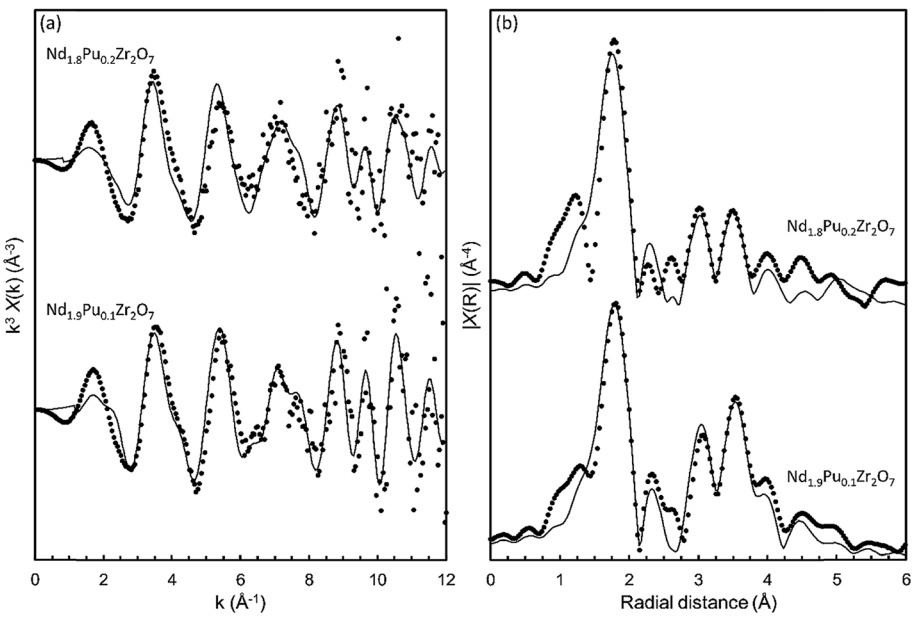

Fig. 6 (a) k^3 weighted Pu L_{III}-edge EXAFS for the pyrochlore samples; (b) the Fourier transform of the EXAFS in R space.

Table 4 Refined structural parameters for the pyrochlore samples from the Pu L_{III} edge EXAFS. The average interatomic distance for a given Pu-i pair is denoted as R (Pu-i), the Debye–Waller factor is denoted as σ^2(i) and the number of scatters in the coordination shell is denoted as N(Pu-i). The fitting range in R was 1.5–5.5 Å and 3.0–11.5 in k. A dash denotes there is no error associated with a value

	$Nd_{1.9}Pu_{0.1}Zr_2O_7$		$Nd_{1.8}Pu_{0.2}Zr_2O_7$	
		±		±
E_0(eV)	5.5	0.9	3.25	1.1
R(Pu–O1$_s$) (Å)	2.29	0.01	2.27	0.02
N(Pu–O1$_s$)	6	—	6	—
R(Pu–O1$_l$) (Å)	2.52	0.03	2.51	0.03
N(Pu–O1$_l$)	2	—	2	—
Avg. R(O1)	2.35	0.03	2.33	0.03
Total N(O1)	8	—	8	—
σ^2(O1) (Å^2)	0.008	0.002	0.008	0.002
R(Pu–Pu) (Å)	3.76	0.04	3.85	0.20
N(Pu–Pu)	0.3	—	0.6	—
σ^2(Pu) (Å^2)	0.012	0.004	0.050	0.080
R(Pu–Nd) (Å)	3.76	0.04	3.85	0.20
N(Pu–Nd)	5.7	—	5.4	—
σ^2(Nd) (Å^2)	0.012	0.004	0.050	0.080
R(Pu–Zr1) (Å)	3.67	0.03	3.63	0.03
N(Pu–Zr1)	6	—	6	—
σ^2(Zr1) (Å^2)	0.010	0.001	0.010	0.002
R(Pu–O2) (Å)	4.06	0.06	3.99	0.04
N(Pu–O2)	12	—	12	—
σ^2(O2) (Å^2)	0.008	0.002	0.008	0.002
R(Pu–O3) (Å)	4.32	0.05	4.73	0.07
N(Pu–O3)	6	—	6	—
σ^2(O3) (Å^2)	0.008	0.002	0.008	0.002
R(Pu–Zr2) (Å)	5.25	0.03	5.23	0.06
N(Pu–Zr2)	6	—	6	—
σ^2(Zr2) (Å^2)	0.010	0.001	0.010	0.002
R (Pu–O4) (Å)	5.55	0.05	5.59	0.07
N(Pu–O4)	12	—	12	—
σ^2(O4) (Å^2)	0.008	0.002	0.008	0.002
R-factor	0.02	—	0.05	—
BVS (v.u.)	3.9	0.1	4.0	0.1

the bond valence sum approach.[46] The bond valence sums determined from the refined EXAFS models were 3.9 ± 0.1 valence units (v.u.) for $Nd_{1.9}Pu_{0.1}Zr_2O_7$, and 4.0 ± 0.1 v.u. for $Nd_{1.8}Pu_{0.2}Zr_2O_7$. Both differ by less than 5% from the formal Pu valence of 4 v.u.

Zirconium k-edge EXAFS. The local structural environment around the Zr atoms was also investigated by quantitative analysis of the EXAFS region of the Zr k-edge data. The structure of $Nd_2Zr_2O_7$ refined by Harvey *et al.*[82] was again used as the starting model. The $Nd_2Zr_2O_7$ pyrochlore structure is characterised by a Zr site in 6-fold coordination, with six Zr–O bond lengths at 2.09 Å. As a first approximation a structural model containing one single scattering path, to represent the six Zr–O1 bonds, was used. The degeneracy of this path was weighted to six and a mean square displacement parameter σ^2(O1) was used to model the thermal vibrations of the nearest neighbour oxygens. This yielded a satisfactory fit to both the $k^3\chi(k)$ waveform and the FT $k^3\chi(k)$ spectral envelope for the $Nd_2Zr_2O_7$ sample. At this stage the fitted k and R ranges were restrained to only model the signal in the FT $k^3\chi(k)$ at approx. 1.6 Å (uncorrected for phase shift). In order to satisfactorily fit the spectral features at higher radial distance, additional scattering paths were added to the model. This took into account the Zr–Nd, Zr–Zr, and Zr–O2 scattering paths at 3.79 Å, 3.80 Å, and 4.09 Å, respectively. As for the first oxygen shell, an appropriately weighted scattering path was chosen to model all like atoms pairs at similar distances. This approach gave a model which provided a good fit (R-factor = 3.0%) to the main features in both the $k^3\chi(k)$ waveform and the FT $k^3\chi(k)$ spectral envelope out to a k of 13 Å^{-1} and an R of 4 Å, respectively. The fits are shown in Fig. 7 and the refined model parameters are shown in Table 5. The data were modelled with nine independent variables: two variables related to the overall EXAFS scattering process ($S_0{}^2$ and E_0) and seven variables related to five independent scattering single scattering path lengths and associated mean squared displacement parameters. The Zr–O1 bond length was determined to be 2.10 Å ± 0.02, which is in good agreement (a difference of 1%) with the weighted mean bond length from the crystal structure published by Harvey *et al.*[82] Independent validation of the refined path lengths can be performed using the bond valence sum approach.[46] The bond valence sum determined from the refined EXAFS model was 3.9 ± 0.1 valence units (v.u.), which differs by less than 5% from the formal Zr valence state of 4 v.u. Comparison of the refined Zr–Nd, Zr–Zr, and Zr–O2 paths defined by EXAFS with the mean contact distances determined by crystallography, showed good agreement between the two techniques.

The same approach was used to fit the EXAFS data from the Pu doped samples. In order to incorporate fractional occupancy of Pu on the A-site, and therefore a contribution from a Zr–Pu scattering path, the model was modified. In order to allow FEFF to generate the additional Zr–Pu scattering path the CIF was modified by changing one of the six second shell neighbours from a Nd atom to a Pu atom. This change alone would result in a fractional occupancy of 0.167 formula units Pu on the A-site. In order to correctly model the fractional occupancy, the contribution (amplitude) of the resulting Zr–Pu scattering path was multiplied by a factor of $x/(1/6)$ and the Zr–Nd scattering paths were multiplied by a factor of $(1-x)/(5/6)$, where x is the fraction of Pu atoms on the A-site. The $(Nd_{2-x}Pu_x)Zr_2O_7$ ($x = 0.1$ and 0.2) data sets were fitted using this modified model with the results shown in Fig. 7 and Table 5. The modified model provided acceptable fits to the EXAFS data with the Zr–O1 paths length determined to be 2.09 Å ± 0.02 and 2.10 Å ± 0.02, for the $x = 0.05$ and 0.10 samples, respectively. This yielded bond valence sums of 3.9 ± 0.1 v.u. and 4.0 ± 0.1 v.u. which were in good agreement with the crystallography. Although the small increases in the Zr–O1 path length is not significant in view of the magnitude of the associated errors, an increase would be expected if the extra oxygen atoms associated with charge balancing the alio-valent substitution of Nd(III) for Pu(IV) were associated with the Zr atoms. Attempts to introduce a contribution from this additional oxygen atom did not significantly improve the quality of the fit. This was not unexpected given that the content of Pu dopant is ten times lower than that of the Zr atoms. Any impact of the extra oxygen on the average Zr–O1 distance would be very small and difficult to detect due to the

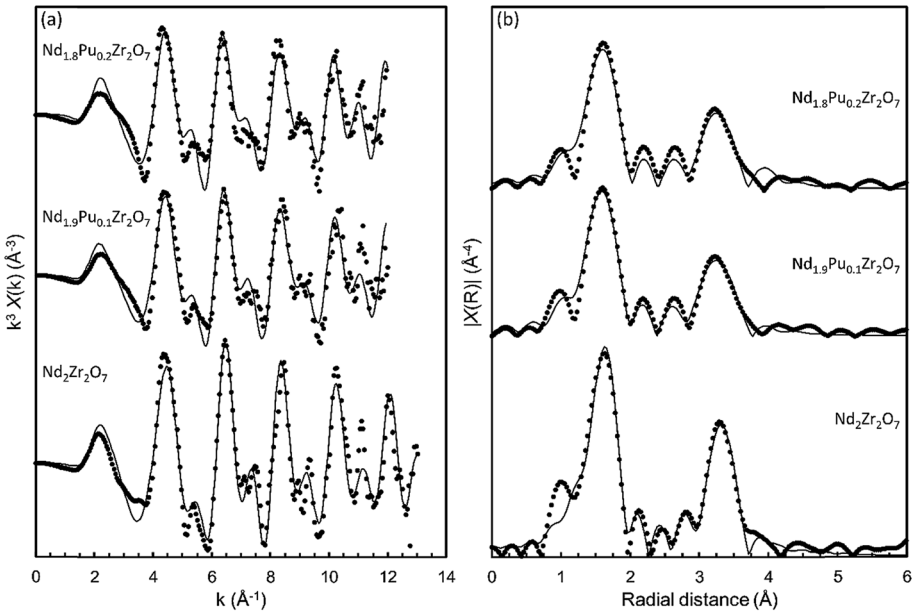

Fig. 7 (a) k^3 weighted Zr k-edge EXAFS for the pyrochlore samples; (b) the Fourier transform of the EXAFS in *R* space.

low occupancy of the vacancy site. The slight increase in the Zr–Nd and Zr–Zr path lengths are not significant given the magnitude of the associated errors. The large increase in the Zr–O2 path length, and the associated errors is consistent with an increase in the overall disorder around the zirconium atoms, as indicated by the analysis of the XANES region.

The immobilisation of Pu(IV) at the eightfold coordinated A site is in contradiction with Pauling's rule, but follows the behaviour described by Verwey and Heilmann.[86,87] Verwey and Heilmann found that the cation with the highest charge adopted the structural site with the highest coordination number in spinels. Based on this, Pu(IV) would be expected to occupy the eightfold coordinated A site in a pyrochlore.

3.4 Molecular modelling

The calculated solution energies of Pu into the $Nd_2Zr_2O_7$ pyrochlore crystal structure, for the reactions given in eqn (2)–(8), are reported in Table 6. The results determined using the force-field method approach of Cleave *et al.*[31] and Perriot *et al.*,[33] are

Table 5 Structural parameters for the pyrochlore samples from the Zr k-edge EXAFS. The average interatomic distance for a given Zr-i pair is denoted as *R*(Zr-i), the Debye–Waller factor is denoted as σ^2(i) and the number of scatters in the coordination shell is denoted as *N*(Zr-i). The fitting range in *R* was 1–4 Å and 3.0–11.5 in *k*. A dash denotes there is no error associated with a value

	$Nd_2Zr_2O_7$		$Nd_{1.9}Pu_{0.1}Zr_2O_7$		$Nd_{1.8}Pu_{0.2}Zr_2O_7$	
		±		±		±
E_0 (eV)	−4.2	1.8	−3.7	1.4	−2.3	1.7
R(Zr–O1) (Å)	2.10	0.02	2.09	0.02	2.10	0.02
N(Zr–O1)	6	—	6	—	6	—
σ^2(O1) (Å^2)	0.004	0.002	0.004	0.003	0.005	0.004
R(Zr–Nd) (Å)	3.79	0.04	3.80	0.03	3.83	0.05
N(Zr–Nd)	6	—	5.7	—	5.4	—
σ^2(Nd) (Å^2)	0.007	0.007	0.005	0.009	0.006	0.010
R(Zr–Pu) (Å)	—	—	3.81	0.03	3.83	0.05
N(Zr–Pu)	—	—	0.3	—	0.6	—
σ^2(Pu) (Å^2)	—	—	0.005	0.009	0.006	0.010
R(Zr–Zr) (Å)	3.80	0.03	3.81	0.03	3.84	0.03
N(Zr–Zr)	6	—	6	—	6	—
σ^2(Zr) (Å^2)	0.004	0.003	0.003	0.005	0.004	0.006
R(Zr–O2) (Å)	4.09	0.09	4.17	0.14	4.25	0.20
N(Zr–O2)	6	—	6	—	6	—
σ^2(O2) (Å^2)	0.004	0.002	0.004	0.003	0.004	0.004
R-factor	0.03	—	0.06	—	0.09	—
BVS (v.u.)	3.9	0.1	4.0	0.1	4.0	0.1

Table 6 The solution energies of Pu in pyrochlore assuming different substitution mechanisms and nominal oxidation states. The charge balance mechanism is indicated in parentheses using Kröger–Vink notation.[88] Note that we computed the energies taking PuO_2 as a reference reactant state for Pu as discussed in Section 2.3. In order to compare the results of different studies[31] the standard enthalpy difference between Pu_2O_3 and PuO_2 of 232 kJ mol^{-1} (2.40 eV)[56] was added to the data of Cleave *et al.*[31] The reported energies are given in eV. In parentheses we report the effect of correlation taken as a difference between the DFT + *U* and DFT values

Reaction	Site	Valence	ΔH_{soln} (eV) DFT (DFT + *U*)	ΔH_{soln} (eV)[31]
2	Nd	Pu(III)	2.37 (−0.03)	2.28
3	Zr($V_O^{\bullet\bullet}$)	Pu(III)	3.02 (+0.05)	>2.28
4	Zr	Pu(IV)	1.33 (+0.11)	0.97
5	Nd(O_v'')	Pu(IV)	1.00 (−0.06)	>0.97
6	Nd(V_{Nd}''')	Pu(IV)	3.83 (−0.06)	>0.97
7	Nd	Pu(III)	1.12 (−0.03)	
8	Zr($V_O^{\bullet\bullet}$)	Pu(III)	1.77 (+0.05)	

also reported for comparison. Both these studies used the same force-field parameters.

The results presented in Table 6 show that the force-field-based solution energies are slightly smaller than the *ab initio* results derived in this work, and that the 5f electrons correlation effects are rather small (*c.a.* 0.1 eV). The results suggest that Pu should be preferentially incorporated on the Nd site as Pu(IV) with an additional oxygen per two Pu atoms occupying an oxygen vacancy (reaction (5)). This prediction of Pu(IV) is in agreement with the analysis of the XAS data. Note that Cleave *et al.*,[31] Perriot *et al.*,[33] and Williford & Weber[32] used Pu_2O_3 as the reference reactant state for Pu, which resulted in a small Pu(III) incorporation energy (−0.12 eV) when Pu(III) occupied the Nd site. The computed DFT energy is −0.01 eV. The approach presented here takes the oxidation step from Pu_2O_3 to PuO_2 (where $\Delta H_{soln} = 2.4$ eV)[56] or the reduction process from Pu(IV) to Pu(III) in the pyrochlore structure, into account.

In order to gain more confidence about the rather surprising inverted bond distances of Pu–O from the EXAFS measurements, these bond distances were computationally derived. The computed Pu–O, Pu–Nd, Pu–Zr and Pu–Pu bond distances for the different structural configurations and oxidation states of Pu in pyrochlore, are reported in Table 7.

It is important to notice that the calculated Pu–O bond lengths are characterised by a set of short (*c.a.* 2.3 Å) and long (*c.a.* 2.5 Å) bonds for the A site. Pu(IV) incorporated on the Zr site has six short bonds, all of the same length, while Pu(IV) incorporated on the Nd site has three short and five long bonds; the configuration consists of two neighbouring Pu atoms and an oxygen atom in an associated vacancy (O_v''). A similar distribution is computed for the case of Pu incorporation on the A site with the formation of an Nd vacancy (V_{Nd}''') to ensure charge neutrality. Incorporation of Pu(III) on the Nd site results in two short and six long bonds. The EXAFS measurements indicate the incorporation of Pu on the Nd site, but with six short (Pu–$O1_s$) bonds and two longer (Pu–$O1_l$) bonds. The calculated bond distances for the scenarios where Pu(IV) occupies the A site are very close to those obtained from experiment. From the calculated solution energies (Table 6) it is energetically highly unfavourable to incorporate Pu(IV) at the A site with charge balance *via* Nd vacancy formation. In fact, the calculated solution energies indicate that Pu(IV) will favourably occupy the A site with charge balance occurring *via* the introduction of oxygen into a former oxygen vacancy. The unexpected results from the EXAFS measurements could indicate a mixture of Pu(IV) on the Nd and Zr sites with approximately equal proportions, which would statistically result in *c.a* 69% of the bonds being of the shorter length (*c.a.* 2.3 Å). This scenario was investigated by modifying the existing EXAFS fitting model to incorporate 50% of the Pu(IV) atoms on each available cation site. Unfortunately, it was not possible to obtain a reliable fit as the model now required more independently refinable variables than could be supported by the information content of the data (Nyquist theorem). This does not definitely preclude this model, however various parameters had to be fixed and the resulting fit yielded large S_0^2 and E_0 values in conjunction with negative mean square displacement parameters.

4. Conclusions

In this paper the fabrication of Pu doped neodymium zirconate pyrochlores *via* a newly developed co-precipitation route is reported. The co-precipitation approach allowed a homogeneous precursor to be formed which facilitates the uniform distribution of Pu at the molecular level. This precursor was subsequently utilised to synthesis single phase materials in the $Nd_{2-x}Pu_xZr_2O_7$ system. Analysis of the XAS data determined the Pu to be incorporated as Pu(IV) on the A-site in the pyrochlore structure. These experimental findings were supported by atomistic simulations which indicate that the lowest solution energy for formation is achieved, when Pu(IV) is substituted on the A-site in the pyrochlore structure, and oxygen atoms are

Table 7 Bond distances (Å) of Pu for four different incorporation scenarios. The degeneracy of a particular bond type is given in parentheses. All values are compared to the experimentally derived bond distances which were derived from the EXAFS fit of the Pu L_{III} edge

Bond	$Pu^{3+}(Pu_{Nd}^{\times})$	$Pu^{4+}(Pu_{Nd}^{\bullet} + 1/3V_{Nd}''')$	$Pu^{4+}(Pu_{Nd}^{\bullet} + 1/2O_v'')$	$Pu^{4+}(Pu_{Zr}^{\times})$	Experiment
Pu–O	2.335 (2)	2.291 (3)	2.301 (3)	2.256 (6)	2.29/2.27 (6)
	2.597 (6)	2.567 (5)	2.485 (5)		2.52/2.51 (2)
Pu–Nd	3.801	3.816/3.782	3.811/3.969	3.819	3.76/3.85
Pu–Zr	3.798	3.756/3.739	3.754	3.798	3.67/3.63
Pu–Pu			3.809		3.76/3.85

introduced at vacancy sites to charge balance. Further analysis showed that the local coordination environment of the Pu(IV) consists of six short and two long Pu–O bonds, which differs from the A site coordination environment in rare earth zirconate pyrochlores. The incorporation of Pu(IV) on the A-site results in significant distortion of the A-site local geometry; this observation is consistent with the smaller ionic radius of Pu(IV), in comparison to Nd(III), and the difference in ionic charge and corresponding crystal field energies. BVS calculations corroborated the calculated bond distances and oxidation state assignment. Analysis by XRD confirmed that the long range structure of the samples was consistent with the pyrochlore structure and confirmed the uptake of Pu(IV) into the structure. The use of precursors generated by novel co-precipitation routes, such as the one reported here, offers the potential for fabrication of samples with an improved degree of chemical homogeneity on a smaller length scales than those produced by more conventional solid state routes.

Conflicts of interest

There are no conflicts to declare.

Acknowledgements

The authors wish to acknowledge the following people: Jessica Bruin, Frodo Klaassen and Paul van den Idsert for assistance with fabricating the Pu doped ceramics at NRG (Petten, NL); Marika Vespa, Jörg Rothe, Kathy Dardenne, Tonya Vitova, and Christian Marquardt for assistance with the sample transportation and support at the INE beamline at ANKA; Tonya Vitova for providing the Pu-reference spectra;[42] Konstantin Rozov for assistance with the GEMS calculations; Tobias Reich and Samer Amayri for providing the design of the sample holder which made the XAS measurements possible; Kurt Sickafus for enlightening discussions. This work was, in part, performed at the synchrotron light source ANKA, which we would like to acknowledge for provision of instrumentation and beamtime. This work was, in part, performed in the MIDAS facility at the University of Sheffield, for which the financial support of the Department of Energy and Climate Change (UK) is gratefully acknowledged. Use of the National Synchrotron Light Source, Brookhaven National Laboratory, was supported by the U.S. Department of Energy, Office of Science, Office of Basic Energy Sciences, under Contract No. DE-AC02-98CH10886. This work was supported, in part, by the UK Engineering & Physical Science Research Council under grants EP/S01019X/1, EP/N017870/1, and EP/R511754/1. The computational resources were provided by the Excellence Initiative of the German federal and state governments and the Jülich-Aachen Research Alliance - High Performance Computing. We thank the JARA-HPC awarding body for time on the RWTH Aachen and FZJ computing clusters awarded through JARA-HPC Partition. Parts of this manuscript are indicated as having already been published in the dissertation of S. Finkeldei entitled "Pyrochlore as nuclear waste form: actinide uptake and chemical stability" 2015.

References

1 R. Vaßen, M. O. Jarligo, T. Steinke, D. E. Mack and D. Stöver, *Surf. Coat. Technol.*, 2010, **205**(4), 38–942.
2 S. T. Norberg, S. Hull, S. G. Eriksson, I. Ahmed, F. Kinyanjui and J. J. Biendicho, *Chem. Mater.*, 2012, **24**(22), 4294–4300.
3 G. R. Lumpkin, K. R. Whittle, S. Rios, K. L. Smith and N. J. Zaluzec, *J. Phys.: Condens. Matter*, 2004, **16**(47), 8557–8570.
4 R. C. Ewing, W. J. Weber and J. Lian, *J. Appl. Phys.*, 2004, **95**(11), 5949–5971.
5 J. P. Icenhower, D. M. Strachan, M. M. Lindberg, E. A. Rodriguez, and J. L. Steele, Report PNNL-14252, 2003.
6 G. R. Lumpkin, *Elements*, 2006, **2**(6), 365–372.
7 B. Burakov, E. Anderson, M. Yagovkina, M. Zamdryanskaya and E. Nikolaeva, *J. Nucl. Sci. Technol.*, 2002, **39**(suppl. 3), 733–736.
8 M. A. Subramanian, G. Aravamudan and G. V. S. Rao, *Prog. Solid State Chem.*, 1983, **15**(2), 55–143.
9 T. Hartmann, A. Alaniz, F. Poineau, P. F. Weck, J. A. Valdez, M. Tang, G. D. Jarvinen, K. R. Czerwinski and K. E. Sickafus, *J. Nucl. Mater.*, 2011, **411**(1–3), 60–71.
10 S. Finkeldei, P. Kegler, P. M. Kowalski, C. Schreinemachers, F. Brandt, A. A. Bukaemskiy, V. L. Vinograd, G. Beridze, A. Shelyug, A. Navrotsky and D. Bosbach, *Acta Mater.*, 2017, **125**, 166–176.
11 Y. Tabira and R. L. Withers, *J. Solid State Chem.*, 1999, **148**(2), 205–214.
12 R. C. Ewing, W. J. Weber and F. W. Clinard, *Prog. Nucl. Energy*, 1995, **29**(2), 63–127.
13 J. Lian, J. Chen, L. M. Wang, R. C. Ewing, J. M. Farmer, L. A. Boatner and K. B. Helean, *Phys. Rev. B: Condens. Matter Mater. Phys.*, 2003, **68**(13), 134107.
14 S. Finkeldei, F. Brandt, K. Rozov, A. A. Bukaemskiy, S. Neumeier and D. Bosbach, *Appl. Geochem.*, 2014, **49**, 31–41.
15 S. Finkeldei, F. Brandt, A. A. Bukaemskiy, S. Neumeier, G. Modolo and D. Bosbach, *Prog. Nucl. Energy*, 2014, **72**, 130–133.
16 K. Holliday, S. Finkeldei, S. Neumeier, C. Walther, D. Bosbach and T. Stumpf, *J. Nucl. Mater.*, 2013, **433**, 479–485.
17 C. Nästren, R. Jardin, J. Somers, M. Walter and B. Brendebach, *J. Solid State Chem.*, 2009, **182**(1), 1–7.
18 D. J. Gregg, Y. J. Zhang, S. C. Middleburgh, S. D. Conradson, G. Triani, G. R. Lumpkin and E. R. Vance, *J. Nucl. Mater.*, 2013, **443**(1–3), 444–451.
19 K. E. Sickafus, L. Minervini, R. W. Grimes, J. A. Valdez, M. Ishimaru, F. Li, K. J. McClellan and T. Hartmann, *Science*, 2000, **289**(5480), 748–751.
20 J. A. Purton and N. L. Allan, *J. Mater. Chem.*, 2002, **12**(10), 2923–2926.
21 A. Chartier, C. Meis, J. P. Crocombette, L. R. Corrales and W. J. Weber, *Phys. Rev. B: Condens. Matter Mater. Phys.*, 2003, **67**(17), 13.

22 A. Chartier, C. Meis, J. P. Crocombette, W. J. Weber and L. R. Corrales, *Phys. Rev. Lett.*, 2005, **94**(2), 025505.
23 A. Chartier, G. Catillon and J. P. Crocombette, *Phys. Rev. Lett.*, 2009, **102**(15), 4.
24 L. Minervini, R. W. Grimes and K. E. Sickafus, *J. Am. Ceram. Soc.*, 2000, **83**(8), 1873–1878.
25 F. X. Zhang, J. W. Wang, J. Lian, M. K. Lang, U. Becker and R. C. Ewing, *Phys. Rev. Lett.*, 2008, **100**(4), 4.
26 W. R. Panero, L. Stixrude and R. C. Ewing, *Phys. Rev. B: Condens. Matter Mater. Phys.*, 2004, **70**(5), 11.
27 L. J. Chen, X. Su and Y. H. Li, First-Principles Study on Cation-Antisite Defects of Stannate and Titanate Pyrochlores, *Open Access Library Journal*, 2014, **1**, e516.
28 Z. J. Chen, H. Y. Xiao, X. T. Zu and F. Gao, *J. Appl. Phys.*, 2008, **104**(9), 6.
29 N. Li, H. Y. Xiao, X. T. Zu, L. M. Wang, R. C. Ewing, J. Lian and F. Gao, *J. Appl. Phys.*, 2007, **102**(6), 6.
30 A. Chartier, C. Meis, W. J. Weber and L. R. Corrales, *Phys. Rev. B: Condens. Matter Mater. Phys.*, 2002, **65**(13), 11.
31 A. Cleave, R. W. Grimes and K. E. Sickafus, *Philos. Mag.*, 2005, **85**(9), 967–980.
32 R. E. Williford and W. J. Weber, *J. Nucl. Mater.*, 2001, **299**(2), 140–147.
33 R. Perriot, P. P. Dholabhai and B. P Uberuaga, *Phys. Chem. Chem. Phys.*, 2016, **18**(33), 22852–22863.
34 Y. Li, P. M. Kowalski, G. Beridze, A. R. Birnie, S. Finkeldei and D. Bosbach, *Scr. Mater.*, 2015, **107**, 18–21.
35 B. P. Uberuaga and R. Perriot, *Phys. Chem. Chem. Phys.*, 2015, **17**(37), 24215–24223.
36 Y. Li and P. M. Kowalski, *J. Nucl. Mater.*, 2018, **505**, 255–261.
37 J. L. Drummond and G. A. Welch, *J. Chem. Soc.*, 1956, 2565–2566.
38 G. H. Bryan, J. K. Thompson, H. H. Van Tuyl, C. L. Brown, and J. L. Ryan, Report BNWL-1941, UC-71, 1976.
39 J. Bruin, personal communication, 2012.
40 S. Finkeldei, Pyrochlore as nuclear waste form: actinide uptake and chemical stability, PhD thesis, Schriften des Forschungszentrums Jülich, Reihe Energie & Umwelt/ Energy & Environment, Jülich, Band/Volume 276, 2015.
41 J. Rothe, M. A. Denecke, K. Dardenne and T. Fanghanel, *Radiochim. Acta*, 2006, **94**(9–11), 691–696.
42 T. Vitova, I. Pidchenko, D. Fellhauer, P. S. Bagus, Y. Joly, T. Pruessmann, S. Bahl, E. Gonzalez-Robles, J. Rothe, M. Altmaier, M. A. Denecke and H. Geckeis, *Nat. Commun.*, 2017, **8**, 16053.
43 B. Ravel and M. Newville, *J. Synchrotron Radiat.*, 2005, **12**(4), 537–541.
44 L. Tröger, D. Arvanitis, K. Baberschke, H. Michaelis, U. Grimm and E. Zschech, *Phys. Rev. B: Condens. Matter Mater. Phys.*, 1992, **46**(6), 3283–3289.
45 J. Goulon, C. Goulon-Ginet, R. Cortes and J. M. Dubois, *J. Phys.*, 1982, **43**(3), 539–548.
46 I. D. Brown and D. Altermatt, *Acta Crystallogr., Sect. B: Struct. Sci.*, 1985, **41**, 244–247.
47 W. H. Zachariasen, *J. Less Common. Met.*, 1978, **62**(C), 1–7.
48 P. Giannozzi, S. Baroni, N. Bonini, M. Calandra, R. Car, C. Cavazzoni, D. Ceresoli, G. L. Chiarotti, M. Cococcioni, I. Dabo, A. Dal Corso, S. de Gironcoli, S. Fabris, G. Fratesi, R. Gebauer, U. Gerstmann, C. Gougoussis, A. Kokalj, M. Lazzeri, L. Martin-Samos, N. Marzari, F. Mauri, R. Mazzarello, S. Paolini, A. Pasquarello, L. Paulatto, C. Sbraccia, S. Scandolo, G. Sclauzero, A. P. Seitsonen, A. Smogunov, P. Umari and R. M. Wentzcovitch, *J. Phys.: Condens. Matter*, 2009, **21**(39), 19.
49 J. P. Perdew, K. Burke and M. Ernzerhof, *Phys. Rev. Lett.*, 1996, **77**(18), 3865–3868.
50 G. Beridze and P. M. Kowalski, *J. Phys. Chem. A*, 2014, **118**(50), 11797–11810.
51 G. Beridze, A. Birnie, S. Koniski, Y. Q. Ji and P. M. Kowalski, *Prog. Nucl. Energy*, 2016, **92**, 142–146.
52 J. P. Perdew, A. Ruzsinszky, G. I. Csonka, O. A. Vydrov, G. E. Scuseria, L. A. Constantin, X. L. Zhou and K. Burke, *Phys. Rev. Lett.*, 2008, **100**(13), 4.
53 D. Vanderbilt, *Phys. Rev. B: Condens. Matter Mater. Phys.*, 1990, **41**(11), 7892–7895.
54 M. Cococcioni and S. de Gironcoli, *Phys. Rev. B: Condens. Matter Mater. Phys.*, 2005, **71**(3), 16.
55 M. Methfessel and A. T. Paxton, *Phys. Rev. B: Condens. Matter Mater. Phys.*, 1989, **40**(6), 3616–3621.
56 R. J. M. Konings, O. Benes, A. Kovacs, D. Manara, D. Sedmidubsky, L. Gorokhov, V. S. Iorish, V. Yungman, E. Shenyavskaya and E. Osina, *J. Phys. Chem. Ref. Data*, 2014, **43**(1), 95.
57 L. M. Toth, H. A. Friedman and M. M. Osborne, *J. Inorg. Nucl. Chem.*, 1981, **43**(11), 2929–2934.
58 W. Hummel, U. Berner, E. Curti, F. J. Pearson and T. Thoenen, *Radiochim. Acta*, 2002, **90**(9–11), 805–813.
59 D. L. Clark, S. S. Hecker, G. D. Jarvinen, and M. P. Neu, Plutonium, *The Chemistry of the Actinide and Transactinide Elements*, ed. L. R. Morss, N. M. Edelstein, and J. Fuger, Springer, Dordrecht, The Netherlands, 2010, pp. 813–1264.
60 S. A. Glazyrin, P. Y. Rodchenko and L. P. Sokhina, *Radiokhimiya*, 1989, **31**(4), 48–52.
61 N. K. Kulkarni, S. Sampath and V. Venugopal, *J. Nucl. Mater.*, 2000, **281**(2–3), 248–250.
62 S. D. Conradson, K. D. Abney, B. D. Begg, E. D. Brady, D. L. Clark, C. den Auwer, M. Ding, P. K. Dorhout, F. J. Espinosa-Faller, P. L. Gordon, R. G. Haire, N. J. Hess, R. F. Hess, D. W. Keogh, G. H. Lander, A. J. Lupinetti, L. A. Morales, M. P. Neu, P. D. Palmer, P. Paviet-Hartmann, S. D. Reilly, W. H. Runde, C. D. Tait, D. K. Veirs and F. Wastin, *Inorg. Chem.*, 2004, **43**(1), 116–131.
63 S. Bertram, G. Kaindl, J. Jové, M. Pagès and J. Gal, *Phys. Rev. Lett.*, 1989, **63**(24), 2680–2683.
64 M. Antonio, L. Soderholm, C. Williams, J. Blaudeau and B. Bursten, *Radiochim. Acta*, 2001, **89**, 17–25.
65 S. D. Conradson, I. Al Mahamid, D. L. Clark, N. J. Hess, E. A. Hudson, M. P. Neu, P. D. Palmer, W. H. Runde and C. Drew Tait, *Polyhedron*, 1998, **17**(4), 599–602.
66 E. A. Hudson, J. J. Rehr and J. J. Bucher, *Phys. Rev. B: Condens. Matter Mater. Phys.*, 1995, **52**, 13815.
67 M. A. Denecke, K. Dardenne and C. M. Marquardt, *Talanta*, 2005, **65**, 1008–1014.

68 A. V. Soldatov, D. Lamoen, M. J. Konstantinović, S. Van den Berghe, A. C. Scheinost and M. Verwerft, *J. Solid State Chem.*, 2007, **180**(1), 54–61.
69 R. G. Haire, P. E. Raison and Z. Assefa, *J. Nucl. Sci. Technol.*, 2002, **39**(suppl. 3), 616–619.
70 S. S. Shoup, C. E. Bamberger and R. G. Haire, *J. Am. Ceram. Soc.*, 1996, **79**(6), 1489–1493.
71 D. A. McKeown, I. S. Muller, A. C. Buechele and I. L. Pegg, *J. Non-Cryst. Solids*, 1999, **258**(1), 98–109.
72 F. Farges, G. Brown and D. Velde, *Am. Mineral.*, 1994, **79**, 838–847.
73 F. Farges, *Geochim. Cosmochim. Acta*, 1991, **55**(11), 3303–3319.
74 G. Mountjoy, D. M. Pickup, R. Anderson, G. W. Wallidge, M. A. Holland, R. J. Newport and M. E. Smith, *Phys. Chem. Chem. Phys.*, 2000, **2**(10), 2455–2460.
75 K. Robinson, G. V. Gibbs and P. H. Ribbe, *Am. Mineral.*, 1971, **56**(5–6), 782.
76 D. K. Smith and H. W. Newkirk, *Acta Crystallogr.*, 1965, **18**(6), 983–991.
77 P. Li, I. W. Chen and J. E. Penner-Hahn, *J. Am. Ceram. Soc.*, 1994, **77**(1), 118–128.
78 S. Ghose and C. Wan, *Am. Mineral.*, 1978, **63**(3–4), 304–310.
79 G. D. Ilyushin, A. A. Voronkov, V. V. Ilyukhin, N. N. Nevskij and N. V. Belov, *Dokl. Akad. Nauk SSSR*, 1981, **260**(3), 623–627.
80 Y.-H. Lee, J.-M. Chen, J.-F. Lee and H.-C. I. Kao, *J. Chin. Chem. Soc.*, 2009, **56**(3), 543–548.
81 P. Li, I. W. Chen and J. E. Penner-Hahn, *Phys. Rev. B: Condens. Matter Mater. Phys.*, 1983, **48**(14), 10063–10073.
82 E. J. Harvey, K. R. Whittle, G. R. Lumpkin, R. I. Smith and S. A. T. Redfern, *J. Solid State Chem.*, 2005, **178**(3), 800–810.
83 R. D. Shannon, *Acta Crystallogr., Sect. A: Cryst. Phys., Diffr., Theor. Gen. Crystallogr.*, 1976, **32**, 751–767.
84 J. J. Rehr, J. J. Kas, M. P. Prange, A. P. Sorini, Y. Takimoto and F. Vila, *C. R. Phys.*, 2009, **10**(6), 548–559.
85 S. R. Hall, F. H. Allen and I. D. Brown, *Acta Crystallogr., Sect. A: Found. Crystallogr.*, 1991, **47**(6), 655–685.
86 E. J. W. Verwey and E. L. Heilmann, *J. Chem. Phys.*, 1947, **15**(4), 174–180.
87 G. R. Lumpkin, M. Pruneda, S. Rios, K. L. Smith, K. Trachenko, K. R. Whittle and N. J. Zaluzec, *J. Solid State Chem.*, 2007, **180**(4), 1512–1518.
88 F. A. Kröger and H. J. Vink, *Solid State Phys.*, 1956, **3**, 307–435.